International Journal of Intelligent Robotics and Applications (2018) 2:400–412
https://doi.org/10.1007/s41315-018-0069-3

REGULAR PAPER

Design and analysis of varied gaits in elastic vibratory milli-robots

Jinhong Qu[1] · **Buyi Zhang**[1] · **Kenn R. Oldham**[1]

Received: 18 July 2018 / Accepted: 25 October 2018 / Published online: 9 November 2018

Abstract
This paper introduces a simple centimeter-scale robot design that uses one or more pairs of piezoelectric, simultaneously-actuated legs to achieve multiple terrestrial gaits, notably jumping and running. The robot is designed for rapid prototyping using a planar geometry that has potential to be transferred to smaller-scales based on micro-fabrication processes, while allowing study of dynamics and control of elastic robot locomotion. Assembled robots are tested in jumping and running, with dynamic responses measured and compared to simulation from a numerical dynamic model. Energy costs of locomotion under various frequency and voltage scenarios are evaluated. Observed behavior emphasizes the impact of synchronizing leg motion in realizing certain gaits, despite the presence of fabrication variability. Scaling of robot dynamics and power consumption is briefly discussed to introduce possible outcomes for future robots manufactured at dimensions representative of microelectromechanical system (MEMS) transducers.

Keywords Micro-robotics · Rapid prototyping · Piezoelectric actuation · Dynamics

1 Introduction

This paper describes a simple rapid-prototyped centimeter-scale robot architecture for study of variable gait opportunities in elastic, planar robots at the meso- and micro-scale. In recent years, the diversity of locomotion options for small-scale robots (millimeters to centimeters in maximum dimension) has grown, with successes in running/walking (Qu et al. 2017; Hollar et al. 2003), crawling (Koh et al. 2010), flying (Wood 2008; Drew and Pister 2017), jumping/hopping (Pierre and Bergbreiter 2017; Haldane et al. 2016; Bergbreiter et al. 2007), and swimming (Li et al. 2009). However, environmental limitations may restrict use of individual locomotion strategies. One strategy to manage limited locomotion capabilities of individual small-scale robots is to rely on multi-robot cooperation. Multi-robot cooperation is realized by coordinating multiple robots using shared (Christensen et al. 2015; Brufau-Penella et al. 2006) or heterogeneous (Rose et al. 2015; Koh et al. 2016) locomotion strategies. However, at small scales, communication availability is often limited, and robots may not easily be able to move to nearby locations.

Robot versatility is potentially improved, whether individually or part of a team, if a robot can utilize different modes of locomotion. This is especially true of robots that can transition between multiple mediums, such as a crawling-jumping robot (Jung et al. 2016) or flying-walking robot (Bachmann et al. 2009). This was recently extended into small-scales with a 175-mg aerial-aquatic robot, with take-off from water in a 14 mm × 6.7 mm × 4.9 mm form factor (Chen et al. 2017). However, significant changes in gait or motion strategy even within a single medium, often sacrificing efficiency or speed for ability to navigate/overcome obstacles, would also enhance small-scale robot capabilities. For example, terrestrial millimeter-scale robots fabricated by micro-electromechanical system (MEMS) techniques have traditionally been constrained to operate on very smooth surfaces by small nominal leg displacements. Hopping, jumping, or even brief flight would greatly enhance mobility, even if those locomotion modes consume momentarily greater power.

The work presented here is intended to explore what can be done to allow different types of terrestrial motions at centimeter and smaller scales, focusing on planar geometries

Electronic supplementary material The online version of this article (https://doi.org/10.1007/s41315-018-0069-3) contains supplementary material, which is available to authorized users.

✉ Kenn R. Oldham
oldham@umich.edu

[1] Department of Mechanical Engineering, University of Michigan, 2350 Hayward St, Ann Arbor, MI 48109, USA

and piezoelectric actuators that may have close analogues in smaller, MEMS-based robots. The current work focuses on a 3 cm wide leg module, exhibiting dynamic running and jumping behaviors.

Prototyping at the centimeter-scale provides two opportunities. First, centimeter-scale terrestrial robots can be functional on their own terms. Many research groups have provided successful designs of either running/walking or jumping robots at centimeter scales (< 10 cm), with select designs compared in Table 1. Among the largest of these robots, electric motors remain powerful enough to move robots very effectively, more than 20 body lengths per second, with steering, in one demonstration (Zarrouk and Fearing 2015), but opportunities remain to increase robot versatility.

Meanwhile, vibratory robots with piezoelectric actuation have also achieved running speeds of several body lengths per second in geometries increasingly more similar to MEMS devices. Hoffman and Wood (2011) presented passive undulatory locomotion to realize biomimetic motion with 20 legs. (Dharmawan et al. 2017) achieved fast locomotion with the ability to steer using different bending vibration modes. Fast locomotion at substantially reduced power was demonstrated in (Rios et al. 2017), with an on-board power unit integrated in (Rios et al. 2018), though at loss of robot velocity. Previous work by the authors (Qu et al. 2017) demonstrated a centimeter-scale robot with a speed of 5 mm/s with detailed modeling of robot and ground contact dynamics; recent work has achieved tethered speed up to 400 mm/s with more aggressive forward motion design (Patel et al. 2018). Other experimental demonstrations of rapid vibratory locomotion from robots < 10 cm in length have also been performed in resonant regimes (Shen et al. 2017; Su et al. 2018).

Among small jumping robots (Haldane et al. 2016) presented a robot capable of jumping more than one meter with electric motor actuation, and (Jung et al. 2016) showed a 10-centimeter robot that could both walk and jump with motor actuation and a mechanical energy storage system.

The second opportunity for centimeter-scale running/walking robots is to serve as prototypes for smaller, typically MEMS-based robots (sub-centimeter length, feature sizes to micron scale). The robot designs presented in (Qu et al. 2017; Dharmawan et al. 2017; Rios et al. 2017), as well as those in this paper, are intended to be scalable for compatibility with micro-fabrication processes, such as that in (Choi et al. 2017). Previous works have performed dynamic modeling of multiple modal vibration behaviors

Table 1 Centimeter-scale running/walking and hopping/jumping robots, characterized by speed (body length/s) and/or jump height (as fraction of body height), with dimensions and power requirements, as available

Design	Actuation	Robot size	Gaits	Performance	Power	Integrated power?
Qu et al. (2017)	Piezoelectric Bimorph	4.4 g; 31.8 × 80 × 0.48 mm^3	Running/walking	0.14 body length/s	< 2.7 mW	No
	Piezoelectric Unimorph	0.44 g; 11 × 22 × 0.12 mm3		0.5 body length/s		
Hoffman and Wood (2011)	Piezoelectric	2.2 g; ~ 100 mm in length	Walking	0.5 body length/s	NA	No
Goldberg et al. (2018)	Piezoelectric	2.8 g, 4.5 cm in length	Running	3.8 body length/s	200 V	Yes
Dharmawan et al. (2017)	Piezoelectric	17.5 g; 50 × 0.5 × 9 mm^3	Running/walking with steering	28 body length/s	1.45 W	No
Pierre and Bergbreiter (2017)	Magnetic	< 2 g; 20 mm in length	Running/pronking	3.9 body length/s 1.47 hip height	25.2 mW	No
Rios et al. (2017)	Piezoelectric	2.86 g; 12.2 × 11 × 9 mm^3	Running/walking	10.8 body length/s	2.49 W	No
Rios et al. (2018)		28 g; 55 mm in length	Running/walking	1.78 body length/s	1.93 W	Yes
Zarrouk and Fearing (2015)	Motor	80 g; 120 mm in length	Running/walking with steering	200 body length/s	0.178 W	Yes
Haldane et al. (2016)	Motor	250 g; 150 mm leg length	Jumping	~4 body height	1.22 J/jump	Yes
Jung et al. (2016)	Motor	59.4 g; 100 mm in length	Walking + jumping	6.3 body length/s ~ 8 body height	2.2 W (walk) 25 J/jump	Yes
This work	Bipedal	0.17 g; 11 × 31.8 × 3 mm^3	Running + jumping	3 body length/s 0.5 body height	46 mW (run) 820 μJ/jump	No
This work	Hexapedal	1.2 g; 21 × 31.8 × 3 mm^3	Running + jumping	8.1 body length/s ~ 0.33 body height	160 mW (run) 1.2 mJ/jump	No

that successfully captured locomotion characteristics near resonances, at both centimeter- and millimeter-scales.

The goal of this paper is to, first, present robot designs with modest abilities for both running and jumping, achieved with extremely low energy requirements and simple, inexpensive fabrication. A second contribution of this paper is to map resonant modeling approaches to a simple form that effectively capture lower-frequency jumping behavior in this modeling framework. Relative to prior works, we seek to provide a relatively simple, dimensionless, and thus easily scalable model that can provide guidance for future robot development. Finally, the paper concludes with discussion of additional implications of multi-gait generation from piezoelectric, elastic structures. These include power consumption results, opportunities for simple control architectures to switch between gaits with low cost-of-transport, and anticipated results if scaled to millimeter, MEMS-based dimensions. This further includes observations of local cost-of-transport optima that we believe expand upon prior works.

2 Robot architecture

We examine robots with size of a few centimeters in their maximum dimension that have predominantly planar structure. These are intended as analogues of smaller, microfabricated robots based on photolithographic patterning on silicon wafers. Consider a simple two-leg example, shown in Fig. 1. The robot chassis, legs, and feet are 3D printed with polylactic acid (PLA). One bimorph lead-zirconate-titanate (PZT) actuator is bonded under the robot body and leg with epoxy, as shown in Fig. 2a. While the predominant deformation of the legs is vertical, an intentional misalignment between the PZT actuator and 3D printed material generates a horizontally-biased motion, which moves the robot forward. The robot stands on the flat bottom of its foot, with some influence from force applied by a wire tethers providing external voltage inputs.

From observation of robot dynamics in previous studies, it was recognized that it is important to synchronize robot legs within elastic terrestrial designs to achieve

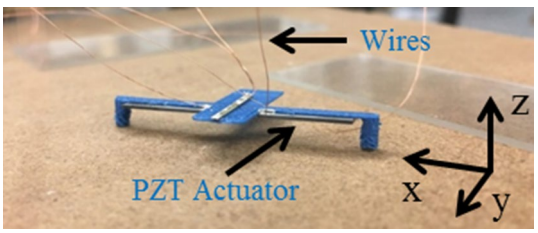

Fig. 1 The photograph of a two-leg robot with PZT intentionally misaligned with its PLA leg. Extra sensing element on top of the body for future test, which is not included in this work

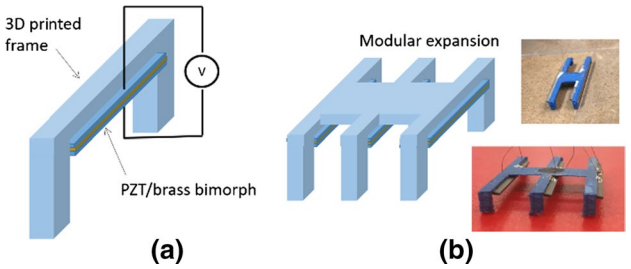

Fig. 2 **a** The basic two-leg module with a shared PZT bimorph can be expanded into (**b**) larger robot assemblies, with four- and six-legged versions, also tested in this work

comparatively uniform motions, as in a jump. Sharing a PZT actuator across the two-leg module provides good synchronization even with modest resolution in manufacturing techniques. After developing gait models for the two-legged prototype, leg modules may be added for improved balance, as in 4- and 6-legged models (with 2 and 3 PZT elements, respectively) as shown in Fig. 2b. Trends in performance as robot size is expanded are discussed in Sect. 5 when examining cost-of-transport and controller design implications.

3 Robot dynamics

3.1 General robot dynamics

A basic model for small, elastic robots with multiple legs can be constructed from a modal vibratory model of the individual legs and a rigid body approximation for the robot body. The legs are assumed to remain in an approximately planar orientation, so that multi-axis rotation may be neglected at the appendage level. Modal dynamics with multiple possible resonances in each leg are then represented in state-space form,

$$\begin{bmatrix} \dot{\mathbf{X}}_{i,i} \\ \vdots \\ \dot{\mathbf{X}}_{n,j} \end{bmatrix} = \begin{bmatrix} \mathbf{A}_1 & & 0 \\ & \ddots & \\ 0 & & \mathbf{A}_n \end{bmatrix} \begin{bmatrix} \boldsymbol{X}_{1,j} \\ \vdots \\ \mathbf{X}_{n,j} \end{bmatrix} + \begin{bmatrix} \mathbf{H}_1 \\ \vdots \\ \mathbf{H}_n \end{bmatrix} \mathbf{F}_{ext,j} \tag{1}$$

where $\mathbf{X}_{i,j}$ is a vector of the modal displacement and velocity of the i-th mode of the j-th leg, $\mathbf{X}_{i,j} = \begin{bmatrix} x_{i,j} & \dot{x}_{i,j} \end{bmatrix}^T$. Dynamics are defined in terms of an effective stiffness, $k_{i,eff}$, damping, $b_{i,eff}$, and modal mass, $m_{i,eff}$, for each mode, collected in state matrix blocks $\mathbf{A}_i$:

$$\mathbf{A}_i = \begin{bmatrix} 0 & 1 \\ -\frac{k_{i,eff}}{m_{i,eff}} & -\frac{b_{i,\mathrm{eff}}}{m_{i,eff}} \end{bmatrix} \tag{2}$$

Rigid body modes for the legs may be included by letting $k_{i,eff}=0$ for the mode to be enumerated. Representative mode

shapes for robot legs of similar geometry have been previously presented graphically in (Qu et al. 2017).

External forces on the elastic leg are treated as acting either in a localized manner at the foot (contact forces, $\mathbf{F}_{tip}$), at the base where it connects to the body (reaction forces and moments, $\mathbf{F}_R$) or distributed along the leg (i.e. piezoelectric actuation, squeeze film damping, $\mathbf{F}_{dis}$). Gains of individual modes in response to each force component are collected as vectors, $\mathbf{h}_{i,tip}$, $\mathbf{h}_{i,R}$, and $\mathbf{h}_{i,dis}$ in the input matrix, $\mathbf{H}_i$, and forces in the combined input vector, $\mathbf{F}_{ext,j}$, for each leg and foot:

$$\mathbf{H}_i = \begin{bmatrix} 0 & 0 & 0 \\ \frac{\mathbf{h}_{i,tip}}{m_{i,eff}} & \frac{\mathbf{h}_{i,dis}}{m_{i,eff}} & \frac{\mathbf{h}_{i,R}}{m_{i,eff}} \end{bmatrix}, \mathbf{F}_{ext,j} = \begin{bmatrix} \mathbf{F}_{tip,j} \\ \mathbf{F}_{dis,j} \\ \mathbf{F}_{R,j} \end{bmatrix} \tag{3}$$

In general, forcing vectors could contain a full six degrees-of-freedom (forces and moments in all three axes). However, the robot foot is treated as a point contact, supporting linear forcing only ($\mathbf{F}_{tip,j} = [f_{tip,x,j}\, f_{tip,y,j}\, f_{tip,z,j}]^T$), and the distributed piezoelectric forcing applies significant excitation only as bending moments ($\mathbf{F}_{dis,j} = [M_{dis,y}\, M_{dis,z,j}]^T$). Further simplifications will be made under assumptions of symmetry and through selection of rigid body mode coordinates in Sect. 3.2.

Displacement of the foot relative to the body in y- and z-axes, $y_{j/b}$ and $z_{j/b}$, is computed from the modal coordinates through an output matrix $\mathbf{C}_j$,

$$\begin{bmatrix} y_{j/b} \\ z_{j/b} \end{bmatrix} = \mathbf{C}_j \begin{bmatrix} \boldsymbol{X}_{1,j} \\ \vdots \\ \mathbf{X}_{n,j} \end{bmatrix} \tag{4}$$

The robot body is treated as rigid with 5 degrees-of-freedom (lateral, or x-axis motion is neglected), with equation of motion

$$\mathbf{M}\ddot{\mathbf{X}}_b + \mathbf{B}\dot{\mathbf{X}}_b = \sum\nolimits_j \mathbf{T}_j \mathbf{F}_{R,j} + \mathbf{F}_b \tag{5}$$

where $\mathbf{M}$ is a mass matrix of robot body mass and rotational inertias, $\mathbf{B}$ is a damping matrix of empirically-determined damping constants, $\mathbf{T}_j$ is a matrix mapping reaction forces and moments at leg j to their effect on the robot center of mass, and $\mathbf{X}_b$ is the vector of the robot body degrees-of-freedom (i.e. $\mathbf{X}_b = [y_b\, z_b\, \theta_{x,b}\, \theta_{y,b}\, \theta_{z,b}]^T$). Vector $\mathbf{F}_b$ contains any robot body forces. A more detailed description of general robot modeling is provided in (Qu et al. 2017).

3.2 Symmetric, low-frequency model approximation

In the authors' previous works on robots of similar architecture (Qu et al. 2017a, b), dynamic locomotion was most effectively predicted near resonant frequencies, though contributions from multiple resonant modes had to be accounted for. This was a consequence of both very limited robot motion without resonant amplification of leg displacement, and of sensitivity of simulated behavior to proper allocation of forces among the multiple modes required to understand dynamic walking/running.

When robots are designed for substantial jumps or hops at low frequency, several simplifications can be made. These are based on the following assumptions:

A1: All robot legs move identically to one other, and thus motion is symmetrical.
A2: Contributions of higher-order resonances can be neglected. Higher-order resonances have been shown previously to be a significant factor in locomotion when miniature robot leg impacts directly influence initial conditions of succeeding steps. However, in this work, they are found to be negligibly excited when robot motion comes nearly to rest between steps. Empirically, this is observed below approximately half the first natural frequency of the robot leg.
A3: Viscous drag on the body is negligible; energy dissipation is dominated by internal losses in the legs and viscous drag on the feet near ground.

A1 is proposed because the robot in this work is built with two legs using a shared PZT strip, which was found to limit synchronization issues empirically. A2 is based on the operating range of our simulation frequencies. From previous work, we found that the higher order resonant modes are important if the actuation frequency is close to or above the first resonant frequency of the actuators. If, as described in this work, the actuation frequency is much lower than the first resonance, than higher order modes can be neglected. A3 is also verified in previous work by comparing the dynamics of centimeter-scale and millimeter scale robots. Under these assumptions (1)–(5) can be approximated by 2-axis translation of a robot body and equivalent foot mass, connected at an angle by the first modal stiffness, shown schematically in Fig. 3. Rotational motions are neglected under A1. Under A2, deformation of a representative leg is defined by its first vibration mode. We choose the dominant modal displacement q, proportional to $x_{1,1}$, to be the distance of the robot foot from its undeformed position, q, reducing (1) and (2) to

$$\begin{aligned} &m_{1,eff}\ddot{q} + b_{1,eff}\dot{q} + k_{1,eff}q \\ &\quad = h_{1,tip,z}f_{tip,z} + h_{1,tip,y}f_{tip,y} + h_{1,dis}f_{dis,eq} \end{aligned} \tag{6}$$

where $h_{1,tip,z}$ and $h_{1,tip,y}$ are the remaining relevant components of $\mathbf{h}_{tip}$ under the symmetry assumptions, and a single equivalent force, $f_{dis,eq}$, is defined to relate the piezoelectric

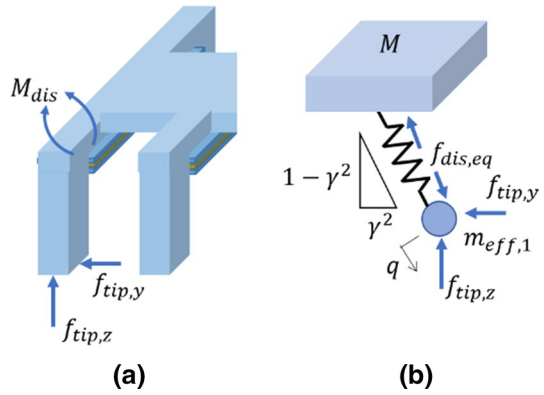

Fig. 3 For low-frequency analysis, **a** generic compliant modal dynamics of legs under external piezoelectric forcing and ground contact forces are approximated by (**b**) equivalent forcing and stiffness at an angle dictated by the first resonant mode shape

bending moments in two axes to linear displacement of the foot from mode 1.

With this selection of modal coordinate, negligible rotation, and higher-order-modes neglected, rigid body

motion of the leg and body may be lumped together together as

$$M\ddot{y}_B = N_j f_{tip,y} \tag{7}$$

$$M\ddot{z}_B = N_j f_{tip,z} - Mg \tag{8}$$

where damping is neglected by A3, M is total leg and body mass, and N_j is the number of legs.

To further simplify analysis, we assume leg deformation and contributions of contact forces to modal excitation are decomposed along the angle, ϕ, of free leg motion (i.e. the angle of the mode shape associated with x_1 or q). Letting $\gamma^2 = \sin(\phi)$, as per Fig. 3b,

$$m_{1,eff}\ddot{q} + b_{1,eff}\dot{q} + k_{1,eff} = h_{1,tip}(1-\gamma^2)f_{tip,z} + \gamma^2 h_{1,tip} f_{tip,y} + h_{1,dis} f_{dis,eq} \tag{9}$$

And tip displacement from (4), A2, and the definition of q becomes

$$y_{tip} = y_B + \gamma^2 q \tag{10}$$

$$z_{tip} = z_B + (1-\gamma^2)q \tag{11}$$

3.3 Non-dimensional dynamics

As simplified in (6)–(10), approximated robot dynamics can be non-dimensionalized for convenient trend analysis. We will analyze robot motion under a square wave with amplitude f_0, i.e. $f_{dis,eq}(t) = f_0\ \mathrm{sign}(\sin(\omega t))$. Then we can non-dimensionalize (8)–(10) based on: a characteristic length, z_{eq}, chosen to be the nominal static displacement of the robot body against gravity,

$$z_{eq} = \frac{h_{1,dis} f_0 - Mg}{k_{1,eff}} \tag{12}$$

a characteristic time or frequency, chosen to be the natural frequency of the first mode,

$$\omega_1 = \sqrt{\frac{k_{1,eff}}{m_{1,eff}}} \tag{13}$$

and a characteristic mass, chosen to be M.

Non-dimensionalized equations of motion become

$$\frac{\delta^2 \xi_y}{\delta \tau^2} = N_j \boldsymbol{\Phi}_y \tag{14}$$

$$\frac{\delta^2 \xi_z}{\delta \tau^2} = N_j \boldsymbol{\Phi}_z - \boldsymbol{\Phi}_g \tag{15}$$

$$\begin{aligned} \frac{\delta^2 \xi_q}{\delta \tau^2} + 2\zeta \frac{\delta \xi_q}{\delta \tau} + \xi_q \quad &= \gamma^2 h_{1,tip} \boldsymbol{\Phi}_y \\ &+ (1-\gamma^2) h_{1,tip} \boldsymbol{\Phi}_z + \boldsymbol{\Phi}_u sign(\sin(\Omega\tau)) \end{aligned} \tag{16}$$

with non-dimensional states $\xi_y = y/z_{eq}$, $\xi_z = z/z_{eq}$, and $\xi_q = q/z_{eq}$, non-dimensional time $\tau = \omega_n t$, non-dimensional forces $\boldsymbol{\Phi}_y = \frac{f_{tip,y}}{M z_{eq}\omega_n^2}$, $\boldsymbol{\Phi}_z = \frac{f_{tip,z}}{M z_{eq}\omega_n^2}$, $\boldsymbol{\Phi}_g = \frac{g}{z_{eq}\omega_n^2}$, and $\boldsymbol{\Phi}_u = \frac{h_{1,dis} f_0}{m_{eff,1} z_{eq}\omega_n^2}$, damping ratio $\zeta = \frac{b_{1,eff}}{2\sqrt{k_{1,eff} m_{1,eff}}}$, and non-dimensional operating frequency, $\Omega = \frac{\omega}{\omega_n}$.

Motion will be assessed by two primary metrics, non-dimensional jumping height at low frequencies:

$$\psi_{z,max} = \max\left\{\frac{z_B(t)}{z_{eq}}\right\} \tag{17}$$

and maximum non-dimensional speed:

$$\psi_{\dot{y},max} = \max\left\{\frac{\delta y_B / \delta t}{z_{eq}\omega_n}\right\} \tag{18}$$

3.4 Contact dynamics and simulation

During motion, the robot foot may be in air ($f_{tip,y} = f_{tip,z} = \boldsymbol{\Phi}_y = \boldsymbol{\Phi}_z = 0$) or experience a contact event. Upon contact, an impulse force is computed based on a coefficient of restitution (CoR), α, under which the foot may rebound or remain in contact. If the foot remains in contact, foot motion becomes constrained ($z_{tip} = 0$, $\dot{y}_{tip} = 0$), reducing the order of the dynamics until $F_{imp,z} < 0$. In either case,

contact forces are dictated by remaining system dynamics. Thus, robot motion is simulated as a hybrid system with two dynamic modes. Outcomes of the simulation are dictated by the remaining dimensional forcing amplitudes, Φ_u (actuator forcing), and Φ_g (gravitational load), as well as coefficient of restitution, α, leg angle, ϕ, and damping ratio, ζ, mass ratio $m_{eff,1}/M$, and operating frequency, Ω.

4 Simulation results

Simulations were initiated using the nominal properties and dimensions of an off-the-shelf PZT bimorph (Piezo System Inc. T219-A4CL-103×PSI-5A4E) and frame fabrication by 3D printing in PLA (Ultimaker 2.0), with robot parameters shown in Table 2. Several simulated trajectories are generated under a given actuation condition, with a 5% resolution error applied to the robot leg properties, such as spring constant and damping ratio, to evaluate the influence caused by variation in fabrication results.

Representative sweeps of non-dimensional jump height and robot speed versus frequency are shown in Fig. 4. There are three main gait behaviors observed, with examples of corresponding vertical foot motion shown in Fig. 5. At very low frequencies ($\Omega < 0.1$, labeled region 1), the robot performs a regular hoping or jumping motion. Some bouncing may occur upon landing, but motion effectively comes to rest before the next step.

Approaching the first resonant frequency ($\Omega > 0.5$, labeled region 3), locomotion is dominated by bouncing impacts of the feat with relatively uniform step height. Peak velocity is predicted near resonance, but accuracy of the simplified model at and beyond this point depends on the proximity of any neglected higher-order modes. In intermediate frequencies (labeled region 2), motion is highly irregular, with substantial bouncing behavior but also short sustained

Table 2 Two-leg robot simulation parameters

Physical parameters	
Robot mass	0.49 g
Robot height	3.2 mm
Robot length	11 mm
Body width	36 mm
PZT actuator size	31.8 mm × 0.48 mm × 3.2 mm
PZT capacitance	4 nF
PZT blocked force	0.08 N
Resonant frequency	923 Hz
Damping constant	1500 (normalized)
Non-dimensional parameters	
Damping ratio, ζ	0.12
CoR, α	0.588
Mode angle, ϕ	10°
Φ_u (at 120 V)	1.04
Φ_g (at 120 V)	0.012

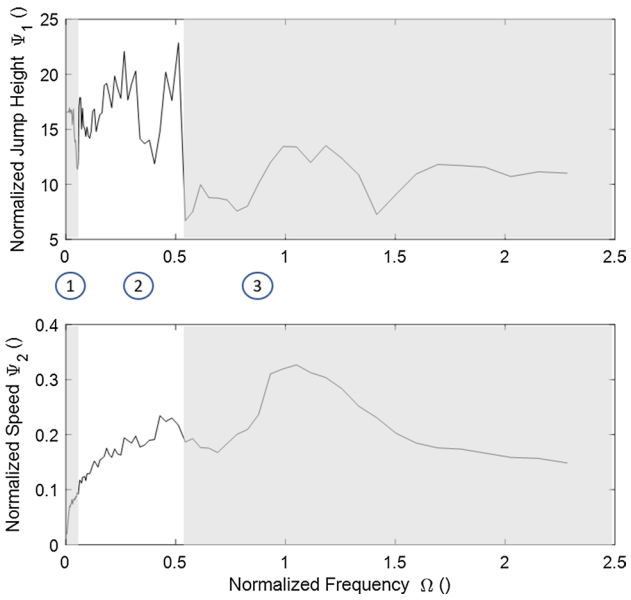

Fig. 4 Representative output amplitudes as a function of frequency, divided into regions of typical dynamic contact behavior, illustrated in Fig. 5; (top) maximum non-dimensional height; (bottom) average non-dimensional speed

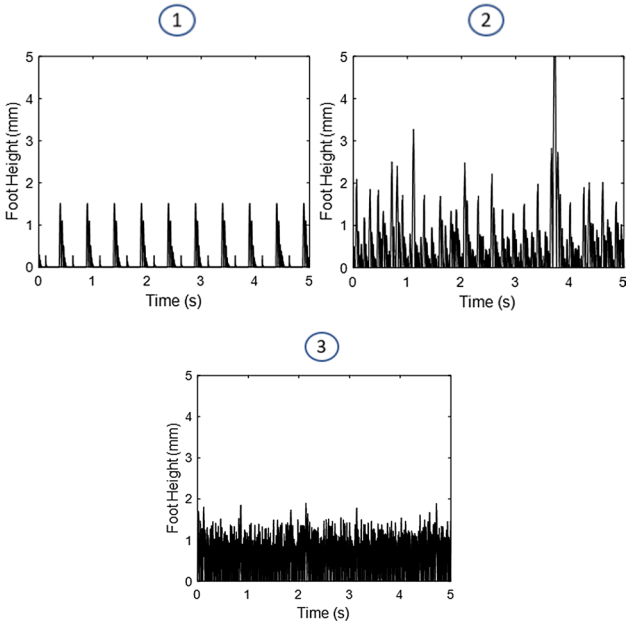

Fig. 5 Representative vertical foot motion from simulation of robot dynamics in various frequency regions (regular hopping, irregular motion with a mix of bouncing and sustained contact, and vibrational "running."

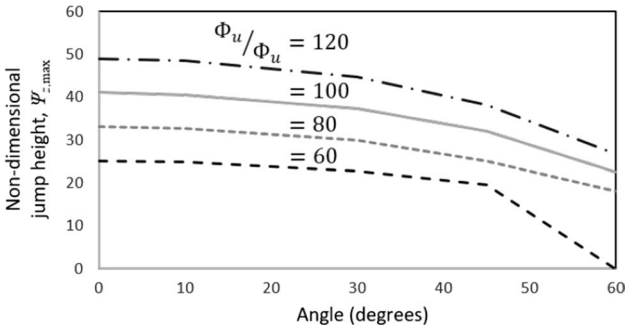

Fig. 6 Jump height compared to static leg displacement ($\Psi_{z,max}$) is decreases gradually with angle of first vibration mode deformation, and increases approximately proportionally with ratio of input forcing to gravitational load (Φ_u/Φ_g)

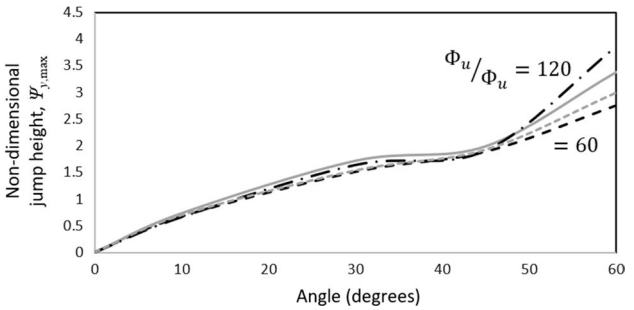

Fig. 7 Maximum running speed based on simplified robot dynamics increases rapidly with first vibration mode angle but is less sensitive to gravitational effects, indicating that speed and static deformation trend proportionally with as input force changes (Φ_u/Φ_g=80,100 unlabeled between curves at 60, 120)

contact, which may interact in complex ways. In simulation, this behavior can give rise to very large jumps, but not in a predictable manner. Simulation results in this region are very sensitive to operating frequency and model parameters.

Focusing on the comparatively predictable regions, predicted trends in behavior are shown for low frequency jump height, $\Psi_{z,max}$ and maximum running speed, Ψ_y in Figs. 6 and 7. Major influences on jump height are the angle of the elastic mode shape, ϕ, and amplitude of forcing, especially relative to gravitational load, Φ_u/Φ_g. Unsurprisingly, large non-dimensional jump heights are associated with near-vertical contact angles and large instantaneous forcing, though large jumps are retained through as reasonable range of angles. In contrast, robot speed increases rapidly with mode angle, but has little separation with varying input to gravitational forcing ratio. This suggests that speed increases nearly proportionally to static leg deformation, per (17), as input forcing increases.

Other non-dimensional parameters have smaller effects on jumping height in simulation. The next most significant factor is the ratio of effective modal mass to total mass; larger modal masses produce larger jumps and faster speeds, but this may be difficult to achieve in practice. Coefficient of restitution and damping ratio, meanwhile, significantly affect running behavior near resonance, but have very little influence on low-frequency jumping. Ground condition effects in general, i.e. coefficient of restitution or surface roughness, primarily affect resonant behaviors, with expanded discussion of these effects available in (Qu et al. 2017).

5 Experimental results

5.1 Fabrication and experimental setup

Robot frames were 3D printed and PZT bimorphs were manually adhered with epoxy. After assembly, fine wire (copper, 40 gauge) was adhered with silver epoxy to the top and bottom electrodes of the PZT ceramics, with at least 20 cm of wire provided to maintain slack between the robot and its power supply.

The actuation signal was provided by a function generator via a voltage amplifier to achieve voltage levels up to 160 V. Before each test, the stress of tethering wires was released to minimize their influence on robot locomotion. Robots were placed on wood and metal surfaces for testing, while the top and/or oblique view of robot motion was recorded at 30 fps with a digital camera. Each robot was tested for locomotion at frequencies ranging from 0 to 160 Hz and voltages from 0 to 200 V. For select tests, velocity of the robot body or legs was measured while passing under a laser Doppler vibrometer.

The three primary types of locomotion predicted in simulation were observed in experimentally. During hopping/jumping, legs remain synchronized and the entire robot departs from ground. During walking/running, the robot body maintains a more consistent height, though there may be instants during running when all feet appear to out of contact with ground, to the resolution of recorded motion. A series of images showing robot walking and open-loop transition to a "jump" is shown in Fig. 8. We note that the two-leg robot does balance successfully on the flat surface of its feet in most experiments, but does receive some intentional aid from the flanges extended in front and behind the legs, and unintentional aid from the wire tethers.

5.2 Measurements

At low frequency, less than 10 Hz ($\Omega \approx 0.1$), the two-legged robot moves slowly but can jump up to half its

body height (2 mm vs. 4 mm). Above a few hundred Hz, the robot has a small probability of jumping, up to at most 1 mm, also similar to predictions based on simulation. Transition from jumping, in which all feet contact ground for

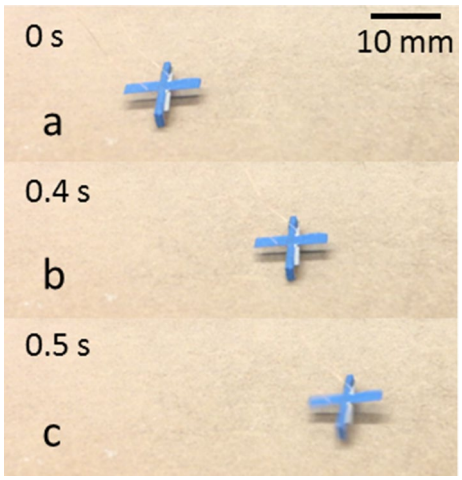

Fig. 8 Sample frame of the robot running and jumping: **a** initial condition before actuation signal; **b** robot position after 0.4 s of running; **c** robot in the middle of an approximately 1.5 mm high jump

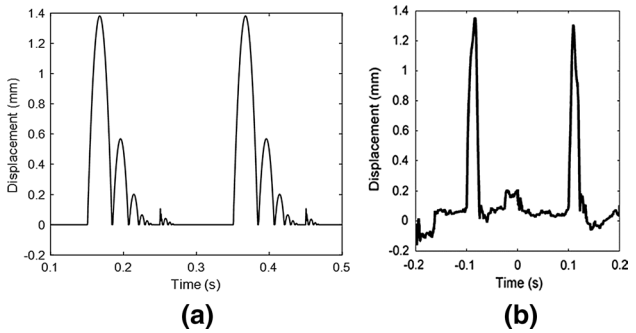

Fig. 9 **a** Simulated and **b** experimental robot vertical motion at 2 Hz, 160 V, with periodical jumping

some finite period, and walking/running without repeatable finite rest, occurred at 15–20 Hz, compared to simulated transition at approximately 10–15 Hz.

Details of sample motions compared to simulation results are shown in Figs. 9, 10, 11 for the 2-leg prototype. Figure 9 shows vertical jumping motion at 2 Hz, 160 V, with nearly identical amplitudes of 1.3 mm. The main discrepancy between simulation and experiments at low frequencies is the presence of more significant bouncing on landing. This may indicate an over-estimated coefficient of restitution. Nonetheless, robot forward speed during jumping is well-modeled, for example that shown in Fig. 10, at 3.9 mm/s in simulation and 4.2 mm/s in experiments with a 5 Hz, 160 V input. Both simulation and experiments capture large incremental jumps forward and additional forward motion between jumps due to leg bending. This latter effect is slightly more pronounced in experiments, possibly due to un-modeled rocking motion.

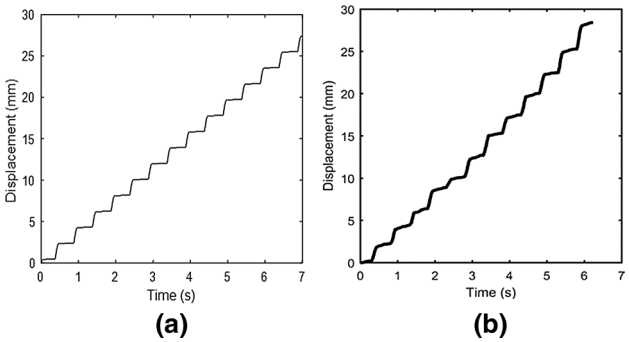

Fig. 10 **a** Simulated and **b** experimental robot forward motion during hopping at 5 Hz, 160 V, showing incremental forward motion at each step

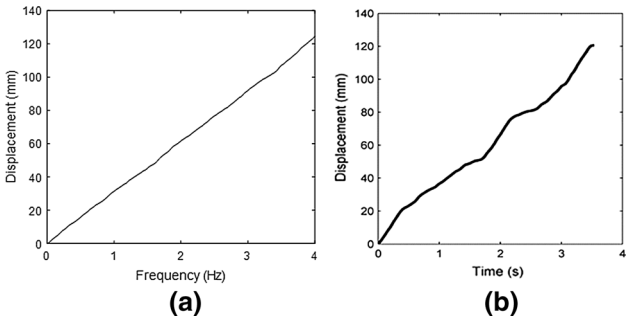

Fig. 11 **a** Simulated and **b** experimental forward motion of robot at 200 Hz, 100 V

For the 2-leg robot, running speeds were also predicted adequately. Figure 11, for example, shows speeds of 30.5 mm/s in simulation and 33.4 ± 4.5 mm/s in experiments, with the major difference being substantially greater variability in real motion, as expected for motion on a non-ideal surface, with roughness and height variation.

As would be expected, the abstracted model in this paper loses effectiveness when higher-order modes have significant contributions to motion. For example, Fig. 12 shows the speed versus frequency behavior of the extended six-leg robot, which had lower first and second natural frequency (~230 Hz, 350 Hz), leading to significant influence of the second vibration mode on resonant running. Low frequency behavior is still modeled well by the simplified model (labeled Sim in Fig. 12), but first resonance behavior begins to deviate from experimental observations (labeled Exp), and second resonance is of course completely un-modeled. Agreement of simulated behavior with experimental results near resonances can be restored by retaining higher-order modes in the model used for simulation, as in (Qu et al. 2017a) and (b), but with loss of comparatively simple non-dimensional trend analysis.

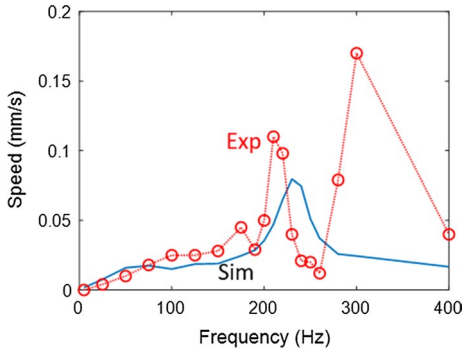

Fig. 12 Speed versus frequency of a six-legged robot at 100 V shows progressively greater deviation between modeled behavior using the single-mode, abstracted model (Sim) and experimental measurements (Exp) as frequencies approach the unmodeled second resonance [experimental data first described in (Zhang et al. 2018)]

6 Discussion

6.1 Energy consumption

Power consumption is a major concern for miniature robots, given limitations of power storage technology and robot payload. The actuation signal in this work is a square wave to a capacitive piezoelectric load, so the major energy dissipation happens when charging the piezoelectric actuators. When the settling time is less than the switching period, the total power dissipation for a given actuation frequency, $f = \omega/2\pi$, is expressed as:

$$P = 2fE_1 \tag{19}$$

in which E_1 is the energy dissipation of a single switch. The single switch dissipation can be further expressed as

$$E_1 = \frac{1}{2}CV^2 \tag{20}$$

in which C is the capacitance of the PZT actuator and V is the actuation voltage.

The actuation current and energy consumption were experimentally measured using a current probe (Tektronix CT6). The total energy dissipation for a single switch was slightly more than 30 μJ for a 20 V input step function. The energy stored on the actuator (E_1) was measured to be more than 7 μJ, versus a calculated value of 3.2 μJ. The mismatch is attributed to parasitic capacitance and other resistive losses in the experimental setup. Therefore, the lower bound of energy dissipation for each individual jump at 2 Hz and 160 V was 819 μJ for the 2-leg robot, which scales proportional to the number of legs. The energy dissipation due to parasitic capacitance might be reduced with an integrated on-board power unit, and a charge recovery circuit (Moon and Jeong 1996) might help to partially recover stored electrical energy lost during switching.

Overall power consumption in experimental regimes, ranging from 1 to 60 mW for cases from 2 Hz at 160 V to 300 Hz at 80 V, can be sourced for minutes to approximately an hour by existing batteries with mass comparable to the robot's own mass (Brightvolt 454523-25XT Data Sheet 2017; Energet Bare Die 2016). However, an integrated power solution for high-voltage supply and control remains a topic of ongoing research (Teichert et al. 2016; Teichert et al. 2018), with progress towards similar loading profiles having been made for applications such as micro-flying insects (Karpelson et al. 2008; Xu et al. 2018). In this work, all experiments were conducted in tethered operation.

6.2 Locomotion efficiency and control implications

An efficiency-like cost-of-transport metric, η, can be easily computed from PZT charging energy based on the number of PZT elements, n_{PZT}, total mass, m_{tot}, and average speed, $\bar{v}$, of the robot at a given frequency and voltage:

$$\eta = \frac{m_{tot} g \bar{v}}{2 n_{PZT} P(f, V)} \tag{21}$$

For the two-legged robot, the wide frequency separation between effective hopping (0-10 Hz) and resonant running (~200 Hz) produces a lower cost-of-transport for hopping, with maximum near $\eta = 0.027$ with a 2 Hz, 160 V inpu, versus $\eta = 0.004$ at 200 Hz, 120 V for the respective gaits. This makes running desirable only when increased speed may be required; the ability to traverse rougher terrain in jumping mode already associated with cheaper cost-of-transport for the two-leg prototype. Cost-of-transport for the two-leg prototype is also not particularly impressive, with $\eta = 0.02$ to 0.18 by this metric for other piezoelectric robots compared in Table 1. This is primarily because most energy is stored in electrically on the PZT elements; but for the two-legged design, this is also a consequence of the low mass of the 2-leg architecture and modest forward velocity. A payload level, operating frequency, and voltage combination would be expected to exist that maximizes cost-of-transport, but was not pursued in this study.

Cost-of-transport becomes more interesting as additional leg units are added. Figure 13a, for example, shows the gaits observed for the 6-legged version (3 PZT elements/leg modules) at various frequencies and voltages. Figure 13b shows a corresponding contour plot of η. As with 2-legs, increasing frequency and voltage produces a transition from hopping (synchronized motion with all legs in air at once) to walking (imperfectly synchronized motion with 1–2 legs on ground at all times) to running (poorly synchronized motion with instances of all legs in air). At very high voltages and

frequencies, the robot's foot impacts become energetic enough to flip the robot over (tumble), even with the wire tethers.

For the 6-leg, 1.2 g robot, local maxima of cost-of-transport exist in all modes, with most efficient locomotion now occurring at a run, and better overall cost-of-transport. Improved running performance ($\eta = 0.117$, at a speed of 17 mm/s) is attributed to a larger mass fraction contributed by the legs/actuators and the robot's ability to better accommodate tilting motion. Hopping performance, however, declines to a maximum height of approximately 1 mm (~ 1/3 body height). In brief, peak jump height declines as synchronization across all legs becomes more difficult to maintain. Very similar behavior is observed for the 4-leg prototype.

One implication of these trends appears to be that maintaining significant hopping height depends heavily on the ability to maintain close symmetry between legs. In contrast, resonant walking or running gaits appear to be sufficiently robust so as to maintain large forward speeds, or even improve forward speed, in the presence of asymmetries. Based on behavior observed for these robots here and in earlier works, this appears to arise from the ability to tune frequencies to balance closely-packed resonant modes of the elastic structure, quite possibly enhanced by other degrees of freedom provided by the robot body (i.e. rocking or tilting).

The existence of local optima for cost-of-transport suggests simple switching control strategies for operating the robot that transition between desirable points for different types of locomotion. For example, Fig. 14 shows a sequence in which a 4-leg robot is operated near its optimal running conditions until forward progress becomes low (in this case blocked). After a given period, the robot tests its hopping gait as a blind attempt to proceed, sacrificing some locomotion efficiency. In the future, feedback signals from integrated of robot sensors, such as antenna (Rudy et al. 2015) or PZT self-sensing at the legs (Zhang et al. 2018) may provide additional information for the robot to make decisions about desirable gait selection. However, it is important to note that real-time control is extremely complex; for example, the two-legged robot is observed to momentarily move backwards in some situations. It is likely most realistic to attempt to control the robot such that periodic inputs provide

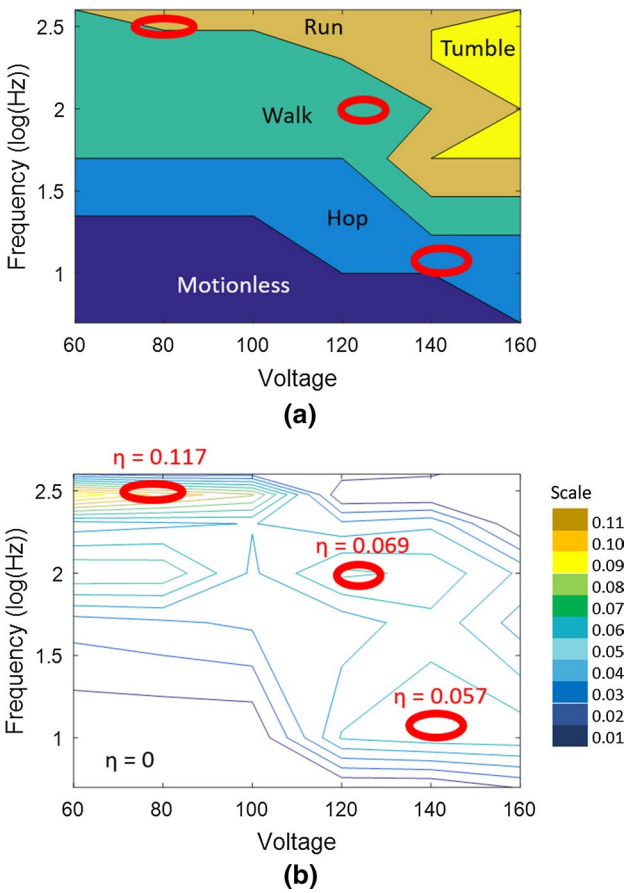

Fig. 13 **a** Observed gait behavior versus frequency and voltage, six-legged robot; **b** contour plot of "efficiency" metric, with local maxima marked, as occurring within various gait regimes

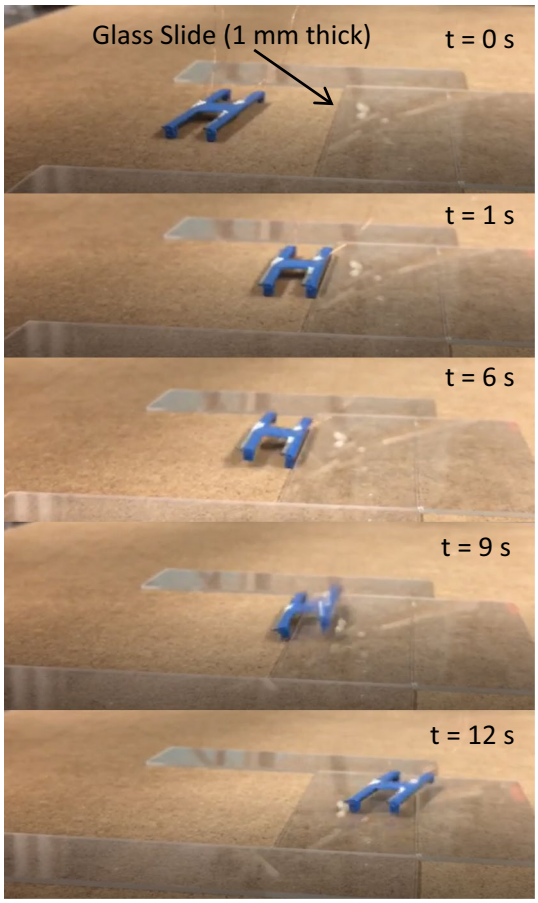

Fig. 14 Naïve switched mode control of a prototype robot, with switching from optimal running excitation to optimal jumping excitation after lack of forward progress for a period of several seconds

a desirable statistical expectation for movement, rather than precise step-to-step positioning.

6.3 Scaling projections

The dynamic model was also modified to provide some prediction of feasible robot locomotion at the millimeter-scale. We hypothesize an identical geometry as the 2-leg robot, scaled by a factor of 10 in all dimensions except for the PZT layer, which is reduced to 1 μm in thickness, reflective of common thin-film PZT dimensions. In non-dimensional modeling terms, this hypothetical 0.49 mg robot corresponds to approximately $\Phi_u = 1.1$, $\Phi_g = 0.018$, and $\Psi_{z,max} = 28$ in the abstracted non-dimensional model. We assume damping ratio, leg tilt angle, and coefficient-of-restitution remain the same at 0.12, 0.588, and 10°, respectively, for the simulation, though prior experience of the authors suggests these would be modestly reduced at micro-scales. We note that for piezoelectric thin-films, large electric fields can be generated at much lower voltages, advantageous for power source and circuit compatibility.

Simulated motion at 20 V, shown in Fig. 15, suggests that such a robot would remain capable of jumping about 2 mm if scaled down as described. This is clearly a simplistic approach, as transitioning to lithography-based methods would also mean transition to different polymer materials (i.e. parylene or PDMS) with greater influence from other thin-films forming the PZT's electrodes, and small-scale forces between the robot foot and ground. Nonetheless, this simulation result suggests that some jumping may be achievable from piezoelectrically-actuated, MEMS-based robots, due to the large work density thin-film piezoelectric materials provide and the elasticity of MEMS structures. Backward motion can be observed in simulation just after some jumps, which can occur either if the foot is still moving forward when the robot strikes the ground, leading a slight backwards rebound at impact, or if oscillation backwards

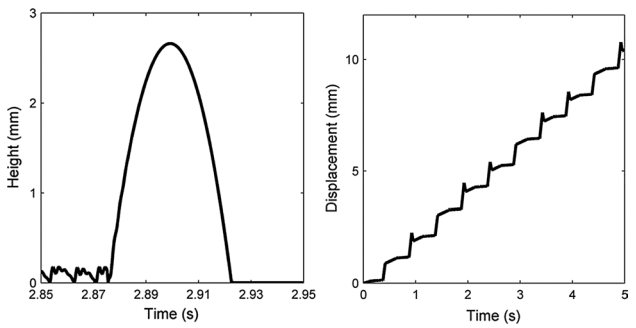

Fig. 15 Robot jumping height and lateral motion simulation for the sample robot geometry if scaled down by 10 times in all dimensions, with piezoelectric forcing calculated for a thin-film PZT layer

of the full body mass when coming to rest leads to slipping behavior at the robot foot.

In practice, as size scales progressively further down, nonlinear small-scale forces will begin to have influence that is not included in the abstracted model presented here. In past works, we have observed effects of squeeze-film damping, adhesive, and electrostatic forces to first become detectable for robots < 0.2 g in mass (Ryou and Oldham 2014) and significant at < 0.5 mg in mass.

7 Conclusion

In this work, we propose a leg architecture, manufactured by simple 3D-printing and piezoelectric actuator assembly at the centimeter-scale to achieve multiple terrestrial locomotion gaits. The leg structure, dynamic modeling methods, and prototype robot evaluation presented in this paper provide one candidate approach for realizing multiple type of locomotion with very small elastic robots. The robot design based on planar processing has potential to be further realized in millimeter scale with existing micro-fabrication technologies. An assembled multi-locomotion robot is presented and tested, with a numerical dynamic model to understand and predict its prominent dynamic motion features.

An initial two-leg robot at the centimeter scale can jump half of its height with low power consumption (819 μJ) for each individual actuation period. The robot is also capable of walking/running up to 34 mm/s, or more than 3 body lengths per second. Speeds of up to 170 mm/s (8 body lengths per second) are achieved when leg modules are cascaded as a quadruped or hexapod. Simulated motion indicates potential for maintaining the disparate gait options and significant jump heights in further miniaturized robots.

With fast running locomotion realized around robot resonance and jumping locomotion at low frequency, the flexibility of small-scale robot navigation of complex terrestrial condition may be increased. A key factor in diversifying motion is the extent to which leg motion can be synchronized despite fabrication variability. One task in future work is to add wobbling motion into the model, which may provide a more accurate jumping height estimate under other actuation conditions. Locomotion switching algorithms should be more formally prepared to make full use of the locomotion capability of the robot, including but not limited to on-board sensing and control algorithms. Switching between advantageous locomotion modes may someday rely on on-board sensing, to help overcome obstacles in the environment.

Acknowledgements The authors thank the National Science Foundation, award CMMI 1435222, for support of this work. The authors also thank Mr. Ketul Patel, Mr. Lu Wang, and Mr. Clark Teeple for their contributions to robot development.

References

Brightvolt Inc.: Brightvolt 454523-25XT Data Sheet, www.brightvolt.com (2017)

Cymbet Corp.: Energet Bare Die, www.cymbet.com (2016)

Bachmann, R.J., Boria, F.J., Vaidyanathan, R., Ifju, P.G., Quinn, R.D.: A biologically inspired micro-vehicle capable of aerial and terrestrial locomotion. Mech. Mach. Theory **44**(3), 513–526 (2009)

Bergbreiter, S., Pister, K.S.: Design of an autonomous jumping microrobot. In: IEEE International Conference on Robotics and Automation, pp. 447–453 (2007)

Brufau-Penella, J., Sánchez-Martín, J., Puig-Vidal, M.: Piezoelectric polymer model validation applied to mm size micro-robot I-SWARM (intelligent swarm). Smart Structures and Materials, pp. 61660Q-61612 (2006)

Chen, Y., Wang, H., Helbling, E.F., Jafferis, N.T., Zufferey, R., Ong, A., Ma, K., Gravish, N., Chirarattananon, P., Kovac, M.: A biologically inspired, flapping-wing, hybrid aerial-aquatic microrobot. Sci. Robot. **2**(11), eaao5619 (2017)

Choi, J., Shin, M., Rudy, R.Q., Kao, C., Pulskamp, J.S., Polcawich, R.G., Oldham, K.R.: Thin-film piezoelectric and high-aspect ratio polymer leg mechanisms for millimeter-scale robotics. Int. J. Intell. Robot. Appl. **1**, 180–184 (2017)

Christensen, D.L., Hawkes, E.W., Suresh, S.A., Ladenheim, K., Cutkosky, M.R.: μTugs: Enabling microrobots to deliver macro forces with controllable adhesives. In: International Conference on Robotics and Automation (ICRA), pp. 4048–4055 (2015)

Dharmawan, A.G., Hariri, H.H., Foong, S., Soh, G.S., Wood, K.L.: Steerable miniature legged robot driven by a single piezoelectric bending unimorph actuator. IEEE International Conference on Robotics and Automation (ICRA), pp. 6008–6013 (2017)

Drew, D.S., Pister, K.S.: First takeoff of a flying microrobot with no moving parts. In: International Conference on Manipulation, Automation and Robotics at Small Scales (MARSS), pp. 1–5 (2017)

Goldberg, B., Zufferey, R., Doshi, N., Heibling, E.F., Whittredge, G., Kovac, M., Wood, R.J.: Power and control autonomy for high-speed locomotion with an insect-scale legged robot. IEEE Robot. Autom. Lett. **3**(2), 987–993 (2018)

Haldane, D.W., Plecnik, M., Yim, J.K., Fearing, R.S.: Robotic vertical jumping agility via series-elastic power modulation. Science Robotics **1**(1), eaag2048 (2016)

Hoffman, K.L., Wood, R.J.: Passive undulatory gaits enhance walking in a myriapod millirobot. IEEE/RSJ International Conference on Intelligent Robots and Systems (IROS), pp. 1479–1486 (2011)

Hollar, S., Flynn, A., Bellew, C., Pister, K.: Solar powered 10 mg silicon robot. In: Micro Electro Mechanical Systems, 2003. IEEE Sixteenth Annual International Conference on MEMS, Kyoyo, pp. 706–711 (2003)

Jung, G.-P., Casarez, C.S., Jung, S.-P., Fearing, R.S., Cho, K.-J.: An integrated jumping-crawling robot using height-adjustable jumping module. IEEE Conf. Robot. Autom. (ICRA), pp. 4680–4685 (2016)

Karpelson, M., Wei, G.-Y., Wood, R.J.: A review of power electronics options for flapping-wing robotic insects. In: IEEE International Conference on Robotics and Automation, Pasadena, CA (2008

Koh, J.-S., Aukes, D.M., Araki, B., Pohorecky, S., Mulgaonkar, Y., Tolley, M.T., Kumar, V., Rus, D., Wood, R.J.: A modular folded laminate robot capable of multi modal locomotion. In: International Symposium on Experimental Robotics pp. 59–70 (2016)

Koh, J.-S., Cho, K.-J.: Omegabot: Crawling robot inspired by ascotis selenaria. IEEE International Conference on Robotics and Automation (ICRA), pp. 109–114 (2010)

Li, H., Tan, J., Zhang, M.: Dynamics modeling and analysis of a swimming microrobot for controlled drug delivery. IEEE Trans. Autom. Sci. Eng. **6**(2), 220–227 (2009)

Moon, Y., Jeong, D.-K.: An efficient charge recovery logic circuit. IEEE J. Solid-State Circuits **31**(4), 514–522 (1996)

Patel, K., Qu, J., Oldham, K.R.: Tilted leg design for a rapid prototyped low-voltage piezoelectric running robot. In: International Conference on Manipulation, Automation, and Robotics at Small Scales, Nagoya (2018)

Pierre, R.S., Bergbreiter, S.: Gait exploration of sub-2 g robots using magnetic actuation. IEEE Robot. Autom. Lett. **2**(1), 34–40 (2017)

Qu, J., Teeple, C.B., Oldham, K.R.: Modeling legged microrobot locomotion based on contact dynamics and vibration in multiple modes and axes. J. Vib. Acoust. **139**(3), 031013 (2017a)

Qu, J., Choi, J., Oldham, K.: Dynamic Structural and Contact Modeling for a Silicon Hexapod Microrobot. J. Mech. Robot. **9**(6), 061006 (2017b)

Rios, S.A., Fleming, A.J., Yong, Y.K.: Miniature resonant ambulatory robot. IEEE Robot. Autom. Lett. **2**(1), 337–343 (2017)

Rios, S.A., Fleming, A.J., Yong, Y.K.: Monolithic piezoelectric insect with resonance walking. IEEE/ASME Trans. Mechatron. **23**(2), 524–530 (2018)

Rose, C.J., Mahmoudieh, P., Fearing, R.S.: Coordinated launching of an ornithopter with a hexapedal robot. In: IEEE International Conference on Robotics and Automation (ICRA), pp. 4029–4035 (2015)

Rudy, R., Cohen, A.J., Pulskamp, J.S., Polcawich, R.G., Oldham, K.R.: Antenna-like tactile sensor for thin-film piezoelectric microrobots. In: ASME International Design Engineering Technical Conferences, pp. V001T009A023 (2015)

Ryou, J.-H., Oldham, K.R.: Dynamic characterization of contact interactions of micro-robotic leg structures. Smart Mater. Struct. **23**, 055014 (2014)

Shen, Z., Liu, Y., Zhao, J., Tang, X., Chen, W.: Design and experiment of a small legged robot operated by resonant vibrations of cantilever beams. IEEE Access **5**, 8451–8458 (2017)

Su, Q., Quan, Q., Deng, J., Yu, H.: A quadruped micro-robot based on piezoelectric driving. Sensors **18**, 810–819 (2018)

Teichert, K., Oldham, K.R.: Characteristics of thin-film batteries cycled over capacitive loads. In: IEEE International Conference on Advanced Intelligent Mechatronics, Banff, AB (2016)

Teichert, K., Oldham, K.R.: Solid-state battery modeling cases studies for the analysis of a micro-robot power system. In: ASME Dynamic Systems and Control Conference, Atlanta GA (2018)

Wood, R.J.: The first takeoff of a biologically inspired at-scale robotic insect. IEEE Trans. Rob. **24**(2), 341–347 (2008)

Xu, Z., Wang, Y., and Chen, C.: Micro converter with a high step-up ratio to drive a piezoelectric bimorph actuator applied in mobile robots. Int. J. Adv. Rob. Syst. pp. 1–9 (2018)

Zarrouk, D., Fearing, R.S.: Controlled in-plane locomotion of a hexapod using a single actuator. IEEE Trans. Rob. **31**(1), 157–167 (2015)

Zhang, B., Qu, J., Oldham, K.R.: Experimental evaluation of piezoelectric self-sensing during terrestrial locomotion of a miniature legged robot. In: IEEE/ASME International Conference on Advanced Intelligent Mechatronics, Auckland (2018)

Jinhong Qu received a B.S. (2011) in engineering physics from the University of Michigan, Ann Arbor, a B.S. (2011) in mechanical engineering from Shanghai Jiao Tong University, Shanghai, China, and the M.S. (2012) and Ph.D. (2017) in mechanical engineering from the University of Michigan, Ann Arbor. His research interests include design, dynamics, modeling, sensing, and control for small scale and MEMS devices. Applications of interest include micro-robotics, inertial sensors, and commercial electronics. He is currently with Apple Inc., Cupertino, CA.

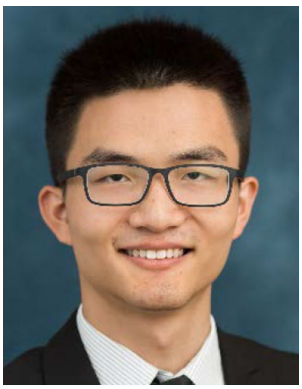

Buyi Zhang received a B.S. (2017) in mechanical engineering from Shanghai Jiao Tong University, Shanghai, China. He is currently a master's student in mechanical engineering and electrical and computer engineering at the University of Michigan, Ann Arbor. His research interests include the sensing and control of micro-robotic systems, electrochemical and thermal modeling and control of lithium-ion battery systems, and signal and image processing with machine learning tools.

Kenn R. Oldham is an Associate Professor of Mechanical Engineering at the University of Michigan, Ann Arbor. Prof. Oldham received the Ph.D. (2006) in Mechanical Engineering from the University of California at Berkeley and a B.S. (2000) in Mechanical Engineering from Carnegie Mellon University. He joined the University of Michigan in 2007 following a postdoctoral fellowship at the U.S. Army Research Laboratory. Prof. Oldham and his research group study the intersection of control systems and micro-scale sensing and actuation, with interests in design for controllability, optimal and robust control, and novel sensor and actuator design. Applications of this research include terrestrial micro-robotics, endoscopic microscopy, and inertial and physiological sensing. Prof. Oldham is currently serving as Associate Chair for Undergraduate Education for Mechanical Engineering and as an Associate Director of the Michigan Center of Integrative Research in Critical Care at the University of Michigan.